Measurement of charged particle yields from PMMA irradiated by a 220 MeV/u ^{12}C beam

2014 Phys. Med. Biol. 59 1857

(http://iopscience.iop.org/0031-9155/59/7/1857)

IOP Publishing | Institute of Physics and Engineering in Medicine Physics in Medicine and Biology

Phys. Med. Biol. **59** (2014) 1857–1872 doi:10.1088/0031-9155/59/7/1857

Measurement of charged particle yields from PMMA irradiated by a 220 MeV/u ^{12}C beam

L Piersanti[1,2], F Bellini[3,4], F Bini[5], F Collamati[3,4], E De Lucia[1], M Durante[6], R Faccini[3,4], F Ferroni[3,4], S Fiore[3], E Iarocci[1,2], C La Tessa[6], M Marafini[3,7], I Mattei[1,8], V Patera[2,4,7], P G Ortega[9,10], A Sarti[1,2], C Schuy[6], A Sciubba[2,4], M Vanstalle[6] and C Voena[3,4]

[1] Laboratori Nazionali di Frascati dell'INFN, Frascati, Italy
[2] Dipartimento di Scienze di Base e Applicate per Ingegneria, Sapienza Università di Roma, Roma, Italy
[3] Dipartimento di Fisica, Sapienza Università di Roma, Roma, Italy
[4] INFN Sezione di Roma, Roma, Italy
[5] Dipartimento di Ingegneria Meccanica e Aerospaziale, Sapienza Università di Roma, Roma, Italy
[6] GSI, Darmstadt, Germany
[7] Museo Storico della Fisica e Centro Studi e Ricerche 'E. Fermi', Roma, Italy
[8] Dipartimento di Matematica e Fisica, Roma Tre Università di Roma, Roma, Italy
[9] CERN, Geneva, Switzerland
[10] IFIC (CSIC/UV), Valencia, Spain

E-mail: vincenzo.patera@lnf.infn.it

Received 7 August 2013, revised 10 February 2014
Accepted for publication 13 February 2014
Published 14 March 2014

Abstract

The radiation used in hadrontherapy treatments interacts with the patient body producing secondary particles, either neutral or charged, that can be used for dose and Bragg peak monitoring and to provide a fast feedback on the treatment plans. Recent results obtained from the authors on simplified setups (mono-energetic primary beams interacting with homogeneous tissue-like target) have already indicated the correlation that exists between the flux of these secondaries coming from the target (e.g. protons and photons) and the position of the primary beam Bragg peak. In this paper, the measurements of charged particle fluxes produced by the interaction of a 220 MeV/u carbon ion beam at GSI, Darmstadt, with a polymethyl methacrylate target are reported. The emission region of protons (p), deuterons (d) and tritons (t) has been characterized using a drift chamber while the particle time-of-flight, used to compute the kinetic energy spectra, was measured with a LYSO scintillator.

The energy released in the LYSO crystal was used for particle identification purposes. The measurements were repeated with the setup at 60° and 90° with respect to the primary beam direction. The accuracy on the fragments emission profile reconstruction and its relationship with the Bragg peak position have been studied. Based on the acquired experimental evidence, a method to monitor the dose profile and the position of the Bragg peak inside the target is proposed.

Keywords: drift chamber, LYSO, hadrontherapy, carbon ion beam, dose monitoring

(Some figures may appear in colour only in the online journal)

1. Introduction

Proton and carbon ion beams are presently used to treat many different solid cancers (Jakel *et al* 2008, Durante and Loeffler 2010) and several new centers based on hadron accelerators are operational or under construction (Amaldi and Kraft 2005, Schardt *et al* 2010). The superior capability of ion therapy to match the maximum dose release with the cancer position requires new and improved dose monitoring techniques, possibly operating during the course of treatment (Knopf and Lomax 2013). This aspect is particularly important for therapy with carbon ion beams, where the dose profile is very sensitive to anatomical changes and minor patients mispositioning.

Most of the methods proposed so far exploit the information provided by the secondary particles produced by the primary ions fragmentation inside the patient's body along their path toward the tumor. Some of them, for example, exploit the correlation that exists between the position of the Bragg peak and the emission profile of fragments created by the beam interaction with the patient body, namely: (i) prompt photons within the 1–10 MeV energy range (Testa *et al* 2008, 2009, Min *et al* 2006, Agodi *et al* 2012a, Bellini *et al* 2014), (ii) pairs of back-to-back photons produced by the annihilation of positrons coming from β^+ emitters (mainly ^{11}C and ^{15}O) (Pawelke *et al* 1997, Parodi *et al* 2002, Enghardt *et al* 2004, Fiedler *et al* 2008, Vecchio *et al* 2009, Attanasi *et al* 2009, Agodi *et al* 2012c), (iii) charged secondary particles, mainly protons, with kinetic energy $E_{kin} \leqslant 150$ MeV/u (Agodi *et al* 2012b, Henriquet *et al* 2012, Gwosch *et al* 2013).

The results reported in literature for the production of charged fragments are obtained with experimental configurations tailored to explore the small angle ($\simeq 30°$, with respect to the beam direction) emission (Henriquet *et al* 2012, Gwosch *et al* 2013). The abundance and energy spectrum of secondary particles emitted by therapeutical beams at large angles with respect to the primary beam direction ($\simeq 90°$) are mainly unknown, and, as a consequence, very poorly reproduced by the nuclear model implemented in the Monte Carlo (MC) codes used to design, for example, dose monitoring devices.

In this paper, we present the results obtained reconstructing secondary charged particles produced during the irradiation of a polymethyl methacrylate (PMMA) target with a 220 MeV/u fully stripped carbon ion beam at GSI, Darmstadt. The flux and energy spectra of protons, deuterons and tritons at different angles with respect to the beam direction (60° and 90°) are reported. A method to correlate the fragments emission profile with the dose distribution delivered in the target and with the beam entrance position is presented.

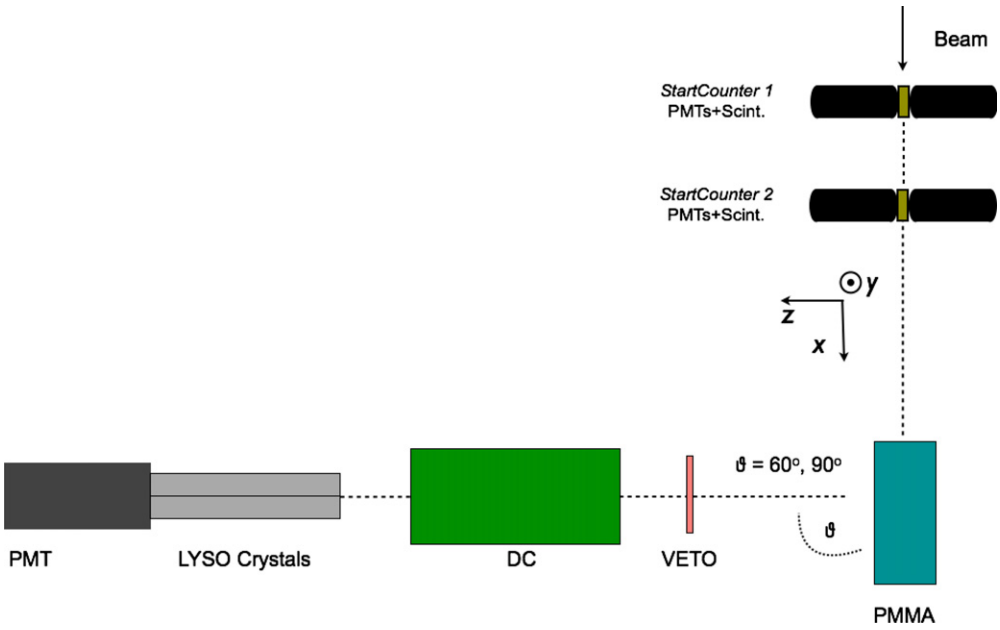

Figure 1. Top view of the experimental setup for the 90° configuration.

2. Experimental setup

A scheme of the experimental setup is shown in figure 1. The data were collected in cave A of the GSI facility using a $20 \times 5 \times 5$ cm^3 PMMA target irradiated with a 220 MeV/u fully stripped ^{12}C beam. The beam spot was Gaussian-shaped, with a standard deviation in the transverse plane $\sigma_{\text{beam}} \simeq 1$ cm, measured with $\sim$1% relative uncertainty by the GSI beam monitor chambers. The beam rate, ranging from hundreds of kHz–$\sim$1 MHz, was monitored by two 1.1 mm-thick plastic scintillators (StartCounter1 and StartCounter2, referred as SC1 and SC2 in the following) placed at 16 and 37 cm upstream of the PMMA target, respectively, and read out by two Hamamatsu 10580 photomultiplier tubes (PMTs). The time and charge information of both start counters were acquired, while only the one closest to the PMMA (SC2) was used to build the trigger signal (taking the OR of the two PMTs).

A scintillation detector, composed of an array of four LYSO crystals, $1.5 \times 1.5 \times 12$ cm^3 each, was placed along the beam line axis at 65.8 cm from the target center. The scintillation light of the crystals was detected with an EMI 9814B PMT.

A 21 cm long drift chamber (DC) (Abou-Haidar *et al* 2012) was placed ahead of the LYSO array at 41 cm from the target center. The experiment orthogonal reference coordinate system, as shown in figure 1, has the x-axis along the incoming beam line, the z-axis in the horizontal plane, and the y-axis in the vertical plane, oriented according to the right-hand rule. The reference frame origin was placed along the x-axis in a fixed position that was, at the beginning of data taking, inside the PMMA at 6.45 cm from the beam entrance surface. The DC center position along the y-axis was mechanically aligned with the target center with a $\leqslant$1 mm precision.

The PMMA was mounted on a single-axis movement stage, connected to a micrometric screw, allowing position scans along the x-axis to be performed with a 0.2 mm accuracy. In the initial configuration the Bragg peak was located on the x-axis at +1.8 cm. Different datasets,

needed to perform the DC calibration, have been collected changing the PMMA position along the beam axis (maximum shift value below 7 mm).

The DC provides a three-dimensional reconstruction of the particle's track using six alternated horizontal (x–z plane V-view) and six vertical (y–z plane U-view) wire layers. The chamber was operated applying the high voltage (HV) to the sense wires (HV = 1.8 kV) and flushing the active volume with an Ar/CO_2 (80/20) gas mixture. The output signals were discriminated applying a 30 mV threshold. In this configuration the single cell spatial resolution is $\leqslant$200 μm and the single cell efficiency is $\simeq$96% (Abou-Haidar *et al* 2012). The readout and performances of the DC and of the LYSO detector have been already reported elsewhere (Agodi *et al* 2012b) as well as the tracking algorithm and DC calibration. Details on the energy and time calibration of the LYSO crystals have also been reported elsewhere (Agodi *et al* 2012c).

A 10 × 10 × 0.2 cm^3 plastic scintillator, marked as VETO in figure 1, is placed between the target and the DC to stop electrons with energy $\lesssim$ 0.55 MeV. During data taking, the LYSO, DC and VETO detectors were mounted on a support that was moved at different angles with respect to the beam direction, allowing the secondary particle-production angular distribution to be studied.

The front-end electronics was read out by a VME system (CAEN V2718 VME-PCI bridge) interfaced with a DELL Precision 9600 PC Data AcQuisition (DAQ) server. The time and charge signals were acquired using 19-bit TDC Multi-hit (CAEN V1190B) and 12-bit QDC (CAEN V792N). The trigger signal was provided by the coincidence, within 80 ns, of the SC2 and of the LYSO detector signals. The threshold used to discriminate the signal from the LYSO PMT (130 mV), is equivalent to 1 MeV when expressed in terms of the energy deposited in the LYSO crystal (E_{LYSO}). The trigger rate, measured at the highest delivered beam rate ($\simeq$2 MHz), was below 1 kHz. The number of incoming carbon ions (N_C) was measured using the logic AND of the signals from the output of the two SC2 PMTs, with a VME scaler (CAEN V560 N) and thus no correction for the DAQ dead time (DT) had to be applied.

The MC simulation of the experimental setup, performed using the FLUKA software (release 2011.2, Ferrari *et al* 2005, Battistoni *et al* 2007) included a detailed simulation of the setup (air included) taking into account the trigger logic, the experimental energy thresholds and the quenching effect in the scintillator (Koba *et al* 2011). The MC sample was hence used to evaluate the setup efficiencies and geometrical acceptances and as a guide for developing and tuning the particle identification (PID). A total number of primary ions $N_C^{60} = 5.26 \times 10^9$ and $N_C^{90} = 2.94 \times 10^9$ for the 60° and 90° configurations, respectively was simulated.

3. Data selection and particle identification

To select events with charged particles that reached the LYSO scintillator we exploited the DC information. The experimental setup was arranged in order to have ions traveling from the target to the LYSO detector and crossing most of the twelve DC tracking planes. Figure 2 shows the measured and simulated distributions of the number of hit cells (N_{hits}) for the 90° configuration, together with the breakdown of the MC distributions obtained for the different hydrogen isotopes.

The MC data have been normalized to the experimental data using the $N_{\mathrm{hits}} = 12$ bin. The peak at $N_{\mathrm{hits}} = 12$ is a clear signature of the charged particles that crossed all the DC planes, firing one cell per plane. The main contribution to the disagreement observed in the $N_{\mathrm{hits}} < 8$ range is the absence of a detailed MC simulation of the electronic cross-talk and of the beam halo induced particle production.

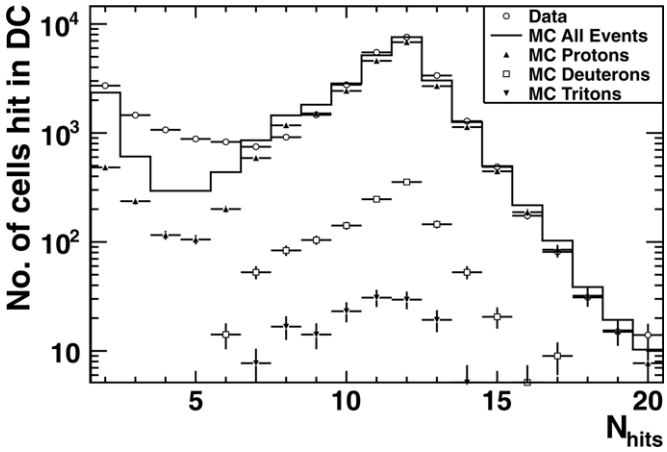

Figure 2. Data (circles) and MC (solid line) distributions of the number of cells hit in the drift chamber (N_{hits}) for events detected by the LYSO crystals ($E_{\text{LYSO}} > 1$ MeV) in the 90° configuration. Individual contributions from protons (up triangles), deuterons (squares) and tritons (down triangles), obtained from the simulation, are also shown. The MC data have been normalized to the experimental data using the $N_{\text{hits}} = 12$ bin.

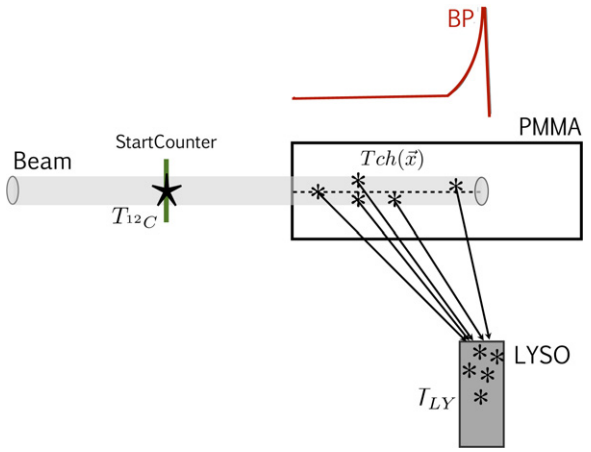

Figure 3. Scheme used for the ToF evaluation (not to scale). The finite beam spot size is shown.

Charged particles were therefore identified with tracks reconstructed in the DC using at least eight N_{hits}, and the isotope discrimination was accomplished combining the LYSO detector time-of-flight (ToF) and scintillation light output information.

3.1. Time-of-flight measurement

The time difference between the SC2 and LYSO signals can be expressed in terms of two different contributions (figure 3): the time required by a carbon ion to travel from the SC2 to the position in the target where a fragmentation occurs ($T_{\text{ch}}(\vec{x})$–$T_{^{12}C}$) and the time needed from the charged fragment to reach the LYSO detector (T_{LY}–$T_{\text{ch}}(\vec{x})$).

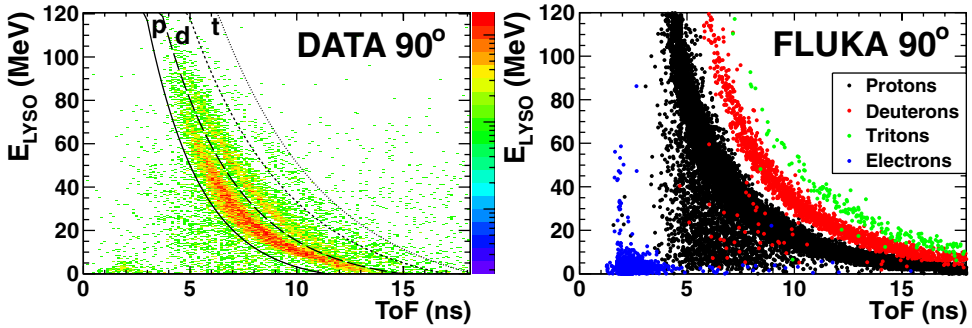

Figure 4. Data (left) and MC (right) distributions of the released energy in the LYSO detector (E_{LYSO}) as a function of the ToF for the 90° setup. The lines used to separate the protons (p), deuterons (d) and tritons (t) in the measured data are superimposed.

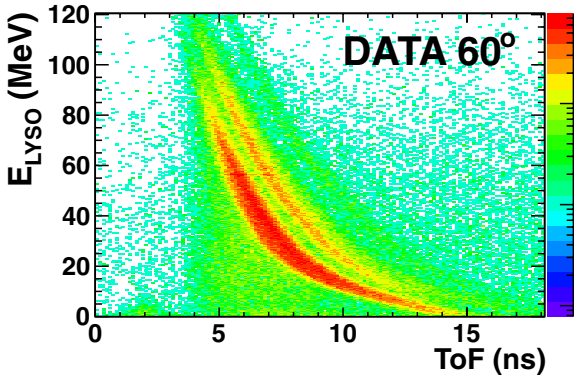

Figure 5. Energy released in the LYSO detector (E_{LYSO}) as a function of the ToF for the 60° configuration.

In order to evaluate the ToF associated to each charged secondary particle, the time required by carbon ions to reach their interaction point in the PMMA target was computed using the full FLUKA MC simulation, and properly taken into account.

3.2. Particle identification

The energy deposited in the LYSO detector as a function of the ToF is shown in figure 4, at 90° for data (left) and MC (right) event samples, while the distribution obtained with the 60° setup is shown in figure 5. The data and MC distributions are showing a similar trend, characterized by three well separated regions for protons, deuterons and tritons, identified in figure 4 (left) by solid, dotted and dashed lines.

The data/MC differences that can be observed in figure 4 can be ascribed to several different factors. First of all, the LYSO crystal calibration, as well as the assessment of the quenching, was performed using radioactive sources and neutron beams providing photons with energies in the range 0.5–10 MeV. Instead the measured charged particle energy distribution spans a wider range up to several tens of MeV. We used a linear calibration for the energy release measurements that does not account for nonlinear contributions or quenching effects.

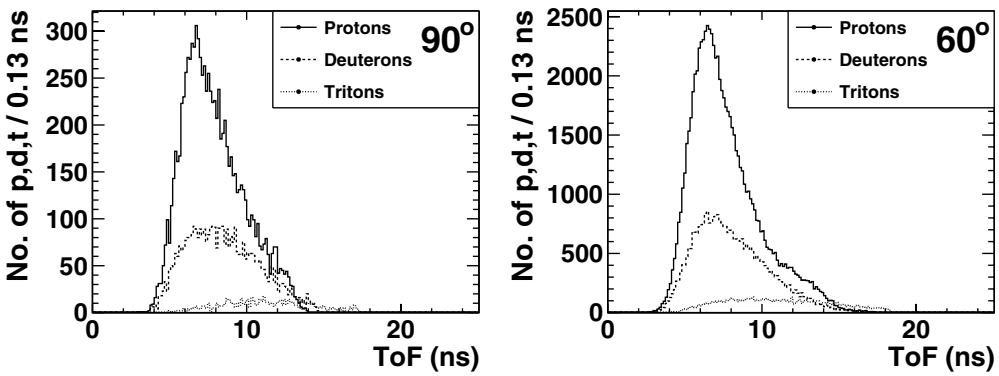

Figure 6. ToF distributions measured for protons, deuterons and tritons in the setup configuration at 90° (left) and 60° (right).

Moreover, in our simplified MC simulation, the charged-particle energy resolution was modeled using calibration measurements performed using photons without accounting for the particle type differences. In addition, the nuclear models driving the charged-particle relative population in the MC simulation are still under development and tuning, with the aim to improve the modest agreement that has already been reported in other published data.

Figure 4 shows the PID selection used in order to separate the three different bands relative to protons, deuterons and tritons. To account for the cross feed among different populations, the separation lines between protons, deuterons and tritons have been moved and a corresponding systematic uncertainty has been evaluated repeating the analysis with the full data sample. This contribution represents the dominating uncertainty on the flux measurement, reaching up to a 23% relative value.

4. The $\beta = v/c$ spectra

Fragments emerging from the patient's body have to cross several centimeters of tissue in order to be detected. Therefore the charged secondary particle β spectra represent an important information for monitoring purposes. The β value distributions were obtained from the ToF spectra shown in figure 6, for all the different charged particles under study.

There are several concurring processes contributing to the observed ToF distribution. First of all, there are different paths, related to different depths of interaction, that the fragments have to travel to reach the LYSO detector from their emission point (see figure 3). The beam spot finite size and the multiple scattering (MS) undergone by the charged particles traversing the PMMA target are additionally smearing the distribution. The different energy loss and slowing down undergone by different isotopes passing through the target needs also to be taken into account when comparing protons, deuterons and tritons spectra.

The simulated spread of the ToF spectrum with respect to the emission velocity (β) is shown in figure 7 for protons, deuterons and tritons.

To take into account all the aforementioned processes, the full MC simulation has been used and the $P^{p,d,t}_{\beta\rightarrow \mathrm{ToF}}$ probability matrix was built using the known values of β and its corresponding ToF (figure 7). Each element of the matrix gives the probability that a particle produced with a given β reaches the LYSO detector with a given ToF, accounting for the uncertainty on ToF evaluated by the MC simulation. Indicating with N^{β}_{j} the number of

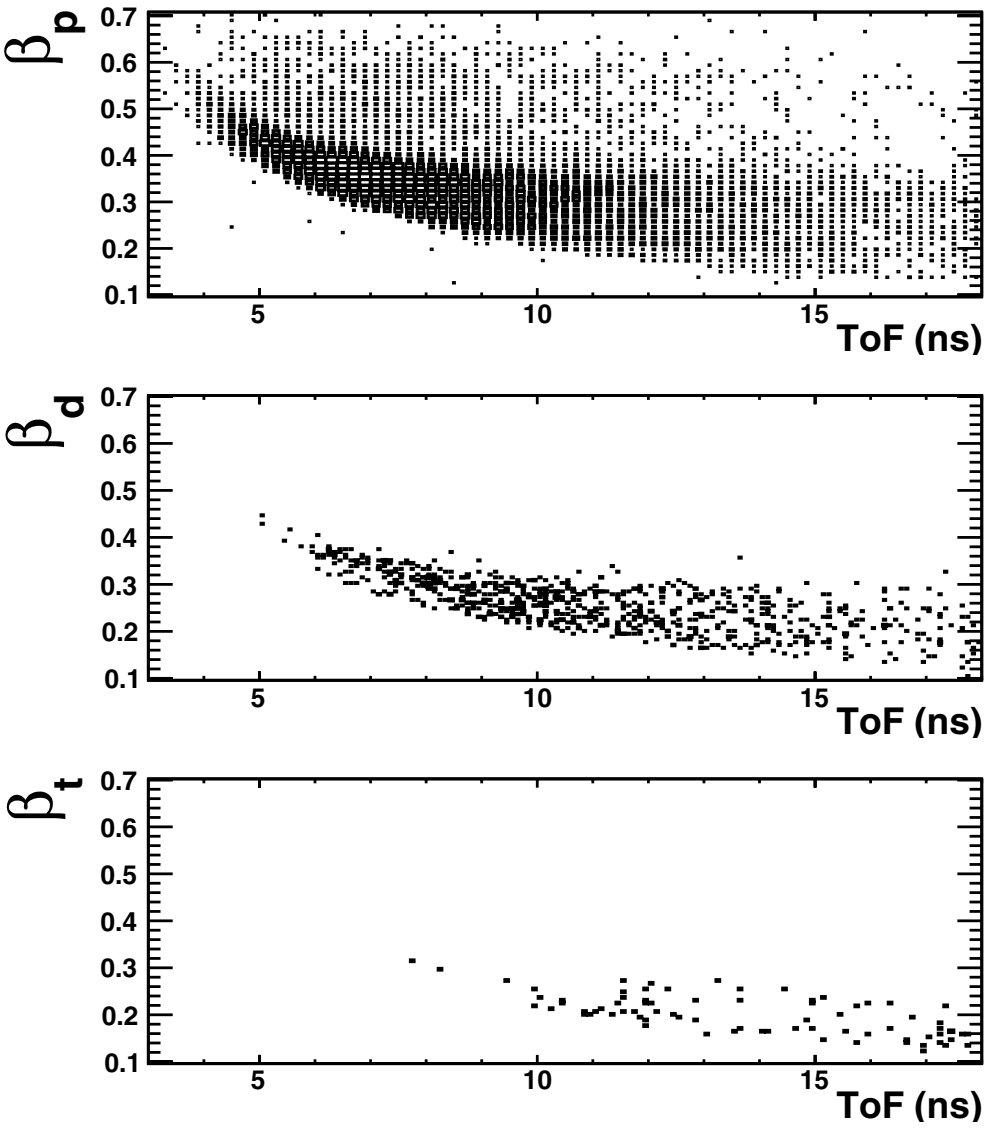

Figure 7. Protons (top), deuterons (middle) and tritons (bottom) β spectra as a function of the ToF according to FLUKA predictions, for the 90° experimental setup.

secondary particles emitted with a velocity β_j and with N_i^{ToF} the number of secondary particles reaching the LYSO detector in a time ToF_i, the following relation holds:

$$N_i^{\mathrm{ToF}} = \sum_j [P_{\beta \to \mathrm{ToF}}]_{ij} \, N_j^{\beta} \tag{1}$$

and has to be inverted in order to extract the β distribution. The final spectra can be obtained from the measured ToF distribution using the following relation:

$$N_j^{\beta} = \sum_i [P_{\beta \to \mathrm{ToF}}]_{ji}^{-1} \, N_i^{\mathrm{ToF}}. \tag{2}$$

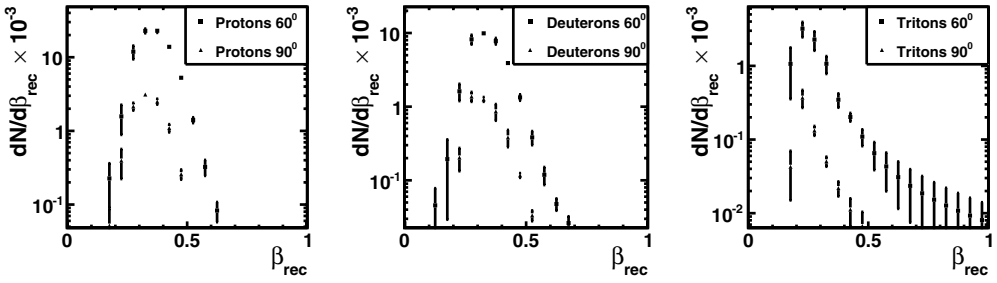

Figure 8. Measured emission velocity (β_{rec}) distributions for protons (left), deuterons (middle) and tritons (right) in the angular configuration at 90° (triangles) and 60° (circles). The error bars show the total (statistical plus systematic) uncertainty.

Equation (2) can be solved with the unfolding procedure described in (Mosegaard and Tarantola 2002), using a probabilistic approach to find the best N_i^{β} configuration minimizing the objective function:

$$\chi^2 = \frac{1}{2}\sum_j \frac{N_j^{\mathrm{ToF}} - \left[\sum_i (P_{\beta\to\mathrm{ToF}})_{ji}\, N_i^{\beta}\right]}{\sqrt{N_j^{\mathrm{ToF}}}}. \tag{3}$$

In this procedure the β and ToF distributions were binned in 20 equally spaced bins, keeping the ToF binning well above the measured time resolution (∼1 ns). The impact on the unfolding result of the chosen binning was evaluated repeating the unfolding procedure while changing the binning (from 10 to 20 bins, with a 1 bin step): the changes in the unfolded spectra were used to assign a systematic uncertainty on β as the RMS of the computed β values for a given measured value (β_{rec}).

Thus the overall uncertainty, shown in figure 8, accounts not only for the limited statistics used in the unfolding, but also for possible data/MC discrepancies in the (ToF, β) plane: by changing the bin size within values always larger than the experimental resolution, the differences in actual spectra of ToF and β in data and MC were tested and the impact on β was measured and accounted for.

The β distributions (β_{rec}) for protons (left), deuterons (middle) and tritons (right) obtained after the unfolding procedure are shown in figure 8, for the setup configuration at 90° (triangles) and 60° (circles) respectively. For each angular configuration, all spectra were normalized to the relative number of isotope species detected by the LYSO crystal. The error bars show the total (statistical plus systematic) uncertainty.

5. Fragments flux

The differential production rate (i.e. *flux*), normalized to the number of incoming carbon ions, for each secondary particle (p, d, t) has been defined as:

$$\frac{\mathrm{d}N_{p,d,t}}{N_C \mathrm{d}\Omega}(\theta) = \frac{1}{N_{\mathrm{C}}}\left[\frac{N_{p,d,t}}{\epsilon_{\mathrm{DT}}\epsilon_{\mathrm{track}}\epsilon_{\mathrm{LYSO}}\Omega_{\mathrm{LYSO}}}\right]^{60^\circ,90^\circ}. \tag{4}$$

The number of protons, deuterons and tritons $N_{p,d,t}$ was measured counting the number of selected tracks after having applied the PID selection (see section 3.2).

The efficiency due to the non-zero DT of the DAQ is shown in equation (4) as ϵ_{DT} and the DC tracking efficiency and the LYSO scintillator detection efficiency are included as $\epsilon_{\mathrm{track}}$ and ϵ_{LYSO}, and were computed using a high-statistics FLUKA MC simulation. The angular

acceptance (Ω_{LYSO}) was measured using the geometrical configuration of the mechanical setup.

The LYSO scintillator detection efficiency was computed for all the different isotopes and angular configurations and found to be within 96–97%, with a negligible statistical uncertainty.

The DC tracking efficiency $\epsilon_{\mathrm{track}}$ was evaluated from the high-statistics MC simulation, requiring at least eight fired cells for each charged track (see section 3). The N_{hits} distribution, shown in figure 2, was used to evaluate the DC tracking efficiency. A systematic uncertainty was assigned by testing the efficiency robustness against variations of the cut on the number of hits. The final result is $\epsilon_{\mathrm{track}} = 93 \pm 3\%$ dominated by systematic uncertainty.

The DT efficiency was computed using the instantaneous event-by-event rate spectra, measured during data acquisition. ϵ_{DT} was obtained fitting the rate spectra in the 50 μs–0.1 ms range, extrapolating the rate in the full 0–0.1 ms range and using the two values to correct for the non-zero DT during data acquisition. Measured values, varying from few %–10%, were found to be in good agreement with the different carbon ion mean rates, ranging from 100 kHz to few MHz, observed during the data taking. The dominant systematic uncertainties on ϵ_{DT} are the fit model and fit range.

The p, d and t measured *fluxes* for the 60° and 90° experimental configurations are:

$$\frac{\mathrm{d}N_p}{N_C \mathrm{d}\Omega}(\theta = 60^\circ) = (8.78 \pm 0.07_{\mathrm{stat}} \pm 0.64_{\mathrm{sys}}) \times 10^{-3}\ \mathrm{sr}^{-1}$$
$$\frac{\mathrm{d}N_d}{N_C \mathrm{d}\Omega}(\theta = 60^\circ) = (3.71 \pm 0.04_{\mathrm{stat}} \pm 0.37_{\mathrm{sys}}) \times 10^{-3}\ \mathrm{sr}^{-1}$$
$$\frac{\mathrm{d}N_t}{N_C \mathrm{d}\Omega}(\theta = 60^\circ) = (0.91 \pm 0.01_{\mathrm{stat}} \pm 0.21_{\mathrm{sys}}) \times 10^{-3}\ \mathrm{sr}^{-1}$$

$$\frac{\mathrm{d}N_p}{N_C \mathrm{d}\Omega}(\theta = 90^\circ) = (1.83 \pm 0.02_{\mathrm{stat}} \pm 0.14_{\mathrm{sys}}) \times 10^{-3}\ \mathrm{sr}^{-1}$$
$$\frac{\mathrm{d}N_d}{N_C \mathrm{d}\Omega}(\theta = 90^\circ) = (0.78 \pm 0.01_{\mathrm{stat}} \pm 0.09_{\mathrm{sys}}) \times 10^{-3}\ \mathrm{sr}^{-1}$$
$$\frac{\mathrm{d}N_t}{N_C \mathrm{d}\Omega}(\theta = 90^\circ) = (0.128 \pm 0.005_{\mathrm{stat}} \pm 0.028_{\mathrm{sys}}) \times 10^{-3}\ \mathrm{sr}^{-1}.$$

The measurements are dominated by systematic uncertainties, with main contributions from PID selection (see section 3.2 for details) and DAQ DT evaluations.

6. Spatial distribution of charged secondary fragments

The spatial distribution of charged secondary fragments can be exploited to monitor the profile of the primary ions deposited dose inside the target. To this aim the production region of charged secondary particles has been studied extrapolating backwards the tracks reconstructed by the DC to the PMMA position on the (x, y) plane (see figure 1), i.e. the plane containing the beam line and the vertical direction. The x and y coordinates of this extrapolation (x_{PMMA}, y_{PMMA}) are providing the projection of the fragments emission point along the primary beam path and along the vertical direction, respectively.

Figure 9 shows the beam penetration into the target as represented by x_{PMMA} and y_{PMMA} from a dataset collected at 90° in the configuration of figure 1, as detailed in section 2, where the beam propagates downwards through the target. The dashed lines indicate the beam entrance position (left, $x^{\mathrm{BE}}_{\mathrm{PMMA}} = -6.450 \pm 0.02$ cm) and the Bragg peak position (right, $x^{\mathrm{BP}}_{\mathrm{PMMA}} = 1.80 \pm 0.02$ cm according to the theoretical calculation).

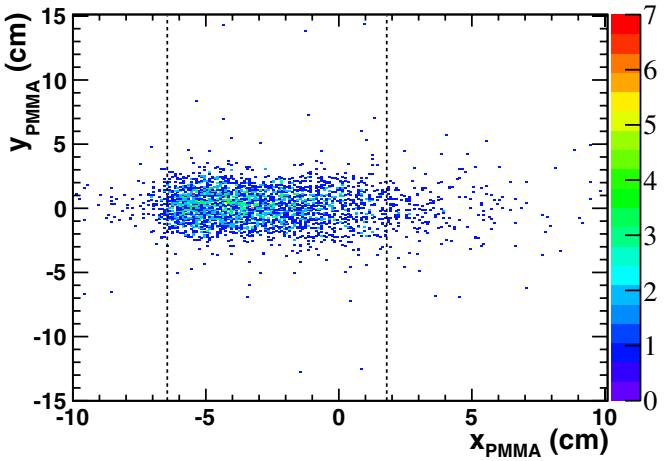

Figure 9. Distribution of the emission points (x_{PMMA}, y_{PMMA}) of the charged secondary particles inside the target for 90° configuration. The vertical dashed lines indicate the beam entrance position in the target (left) and the theoretical calculation of the Bragg peak position (right), respectively.

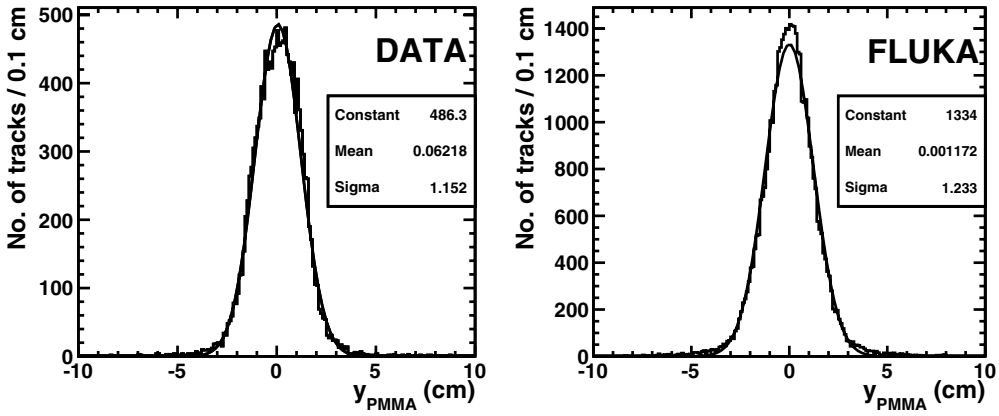

Figure 10. Measured (left) and simulated (right) vertical profile of fragments at their emission point inside the target for the 90° data sample.

The measured and simulated y_{PMMA} profiles are shown in figure 10 for the 90° experimental configuration. The y_{PMMA} distribution shows the reconstructed transverse beam profile in the vertical direction. This distribution can be used to evaluate the MS suffered by the fragments inside the target knowing the beam spot size $\sigma_{\mathrm{beam}} = 1$ cm as provided, with $\sim$1% relative uncertainty, by the GSI beam monitors.

Since the shape of the fragments vertical profile is a convolution of the primary beam profile, the MS contribution (σ_{MS}) and of the tracking resolution, the latter has been studied in detail in order to be properly subtracted, if needed.

The DC tracking resolution, evaluated at the emission point (at nearly 40 cm from the DC center), is $\sim$1.1 mm and has been computed using the covariance matrix of the reconstructed charged track parameters, together with the single track resolution ($\simeq$200 μm) measured at the DC center.

The measured value of σ_{MS} is obtained from $\sigma_{\mathrm{MS}} = \sqrt{\sigma_y^2 - (\sigma_B^2)} \simeq 6$ mm where $\sigma_y = 1.153$ cm (from figure 10), the beam spot size is $\sigma_B = 10$ mm and the tracking contribution ($\sim$1.1 mm) is neglected. The MS contribution to the resolution can increase up to a factor 2–3 in a patient treatment real-case scenario, scaling with the square root of the tissue thickness traversed by the particles.

The choice of the θ angle value at which a monitoring detector should be placed with respect to the primary beam direction appears to be crucial in any dose profile monitoring application. Such angle, heavily depends on the spatial distribution of the charged secondary fragments.

At small detection angles, the emission flux is enhanced and the energy spectrum of the charged particles is harder, thus maximizing the statistics and minimizing the MS of p, d and t inside the patient. On the other hand, the spatial resolution on the emission shape worsens as $(\sin\theta)^{-1}$, due to the projection along the beam line, and this effect could become dominant for small detection angles. Several effects are present at a given angle, like the MS of the track in the PMMA and the projection (shadow) of the beam spot on the beam line. In order to take these effects properly into account a $\simeq \sigma_{\mathrm{beam}} \times \cot(\theta)$ term has to be included in the description of the emission profile. And since these two terms are increasing with decreasing detection angle (θ), a better tracking accuracy, from a geometrical point of view, can be obtained at large θ values.

Figure 12 (left) shows the measured longitudinal emission distribution x_{PMMA} for all the detected charged particles using the data sample collected at 90° (solid line) with the superimposed depth-dose profile calculated with FLUKA (hatched distribution). A clear correlation between the rising edge of the x_{PMMA} distribution and the beam entrance position in the target can be observed. The relationship of the charged emission profile, and in particular of the profile falling edge, with the position of the Bragg peak can provide a method to monitor the dose release and the Bragg peak position. As shown in figure 12 (right), the distribution can be well described by the function:

$$f(x) = p_0 \frac{1}{1 + \exp\left(\frac{x-p_1}{p_2}\right)} \frac{1}{1 + \exp\left(-\frac{x-p_3}{p_4}\right)} + p_5. \tag{5}$$

Parameters p_3 and p_1 are related to the rising and falling edge of the distribution, respectively, while p_4 and p_2 describe the rising and falling slopes of the function. A flat background contribution is modeled through the parameter p_5. The beam shadow has been explicitly added as a convolution of a Gaussian function with $\sigma \simeq \sigma_{\mathrm{beam}} \times \cot(\theta)$. This function was able to describe all the emission profiles measured for different isotopes and data samples taken with different geometrical conditions (beam entrances) and angle configurations (60° and 90°).

Two quantities, Δ_{40} and δ_{40} have been defined, as shown in figure 12 (right), to characterize the longitudinal particle profile. Δ_{40} represents the width of the $f(x)$ distribution at 40% of its maximum with X_{left} and X_{right} being respectively the corresponding x values at the rising and falling edges. δ_{40} is instead the distance between X_{left} and the x-intercept of the tangent to $f(x)$ at $x = X_{\mathrm{right}}$.

The accuracy of this method in monitoring the Bragg peak position is influenced by several elements: the MS suffered by the fragments inside the patient, the statistics of the collected sample and the intrinsic fluctuation of the emission process related to the nuclear interactions.

This last contribution has been investigated for a fixed number (10^3) of detected fragments. Out of the datasets acquired at each angular configuration, samples of 10^3 tracked charged fragments were produced (13 samples at 90° and 100 samples at 60°) and the corresponding values of Δ_{40} and δ_{40} were measured. When comparing measurements of Δ_{40} and δ_{40}

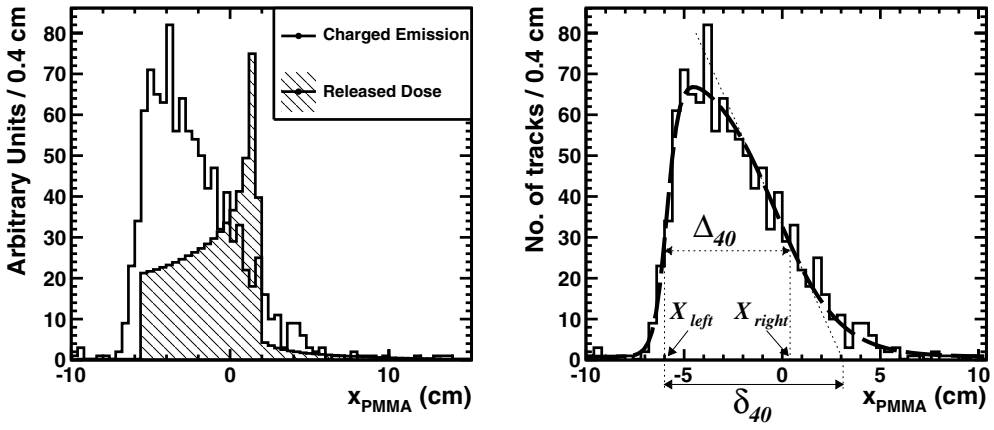

Figure 11. Left: simulated depth-dose distribution (hatched) superimposed on the longitudinal profile (solid line) of charged secondary particles as a function of x_{PMMA} at 90°. Right: longitudinal profile of charged fragments inside the target at 90°, from a dataset collected with beam entrance at −6.15 cm. The PDF from equation (5) is superimposed. The dotted and solid arrows show the graphical representation of Δ_{40} and δ_{40} respectively. The variables X_{left} and X_{right} are also shown.

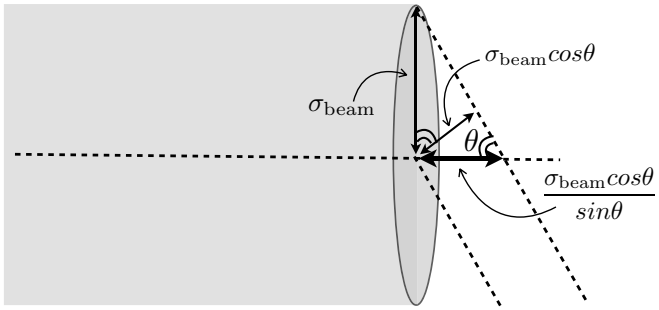

Figure 12. Scheme of the beam spot size and its contribution to the reconstruction of the fragments emission region with the experimental setup placed at the angle θ with respect to the primary beam direction.

Table 1. Values and dispersion of the Δ_{40} and δ_{40} variables. The resolutions (σ), for each angle configuration, are evaluated as the RMS of the delta distributions measured in the different beam entrance configurations and data samples.

Angle (deg)	σ_{Δ} (cm)	σ_{δ} (cm)	$\sigma_{X_{\mathrm{left}}}$ (cm)	$\overline{\Delta_{40}}$ (cm)	$\overline{\delta_{40}}$ (cm)
90	0.34	0.37	0.08	6.60 ± 0.09	9.40 ± 0.10
60	0.31	0.28	0.09	6.83 ± 0.03	9.44 ± 0.03

performed at different angles, the finite spot size of the beam σ_{beam} (figure 11) was taken into account.

The precision on the measurement of the Δ_{40}, δ_{40} and X_{left} together with the average values of Δ_{40} and δ_{40} are shown in table 1. The measured values of Δ_{40} and δ_{40} should be compared with the path $\Delta_{\mathrm{beam}} = 8.90 \pm 0.03$ cm, traveled by the primary beam from its

entrance position in the target to the Bragg peak position that was determined from the MC simulation (GEANT) used by the GSI beam setup and calibration team.

The application of such technique to the 'online' monitoring (in-treatment) of the beam path inside a patient, would require a calibration of the measured δ_{40} and Δ_{40} values against all the different Δ_{beam} paths related to the different pencil beam energies and beam penetration depths.

Beside the monitoring of the Bragg peak position, the proposed technology would provide also some useful information related to the patient positioning. By measuring the beam entrance position in the patient, correlated to X_{left} and whose accuracy is listed in table 1, it will be possible to provide a fast and precise feedback on possible patient mispositionings during the treatment.

The reference sample (10^3 fragments) used to validate the performances of the monitoring technique proposed in this paper, according to the measured values reported in section 5, can be produced in a $\Delta\Omega \simeq 10^{-4}$ sr solid angle by a number of carbon ions impinging on the PMMA target equal to $\simeq 2.3 \times 10^8$ at 90° and to $\simeq 4.7 \times 10^7$ at 60°.

To make a comparison with a standard carbon ion treatment, considering a single pencil beam reaching the distal part of the tumor for which the monitor capability along the beam line is crucial, the ion density will be of the order of 10^8 carbon ions per cm^3. As a full treatment involves several different pencil beams, each one will contribute to the overall reconstructed emission shape with its own emission pattern. It is then crucial to maximize the geometrical acceptance of the monitor device in order to collect the desired tracks sample minimizing the superposition of different pencil beams, targeting different voxels.

7. Discussion and conclusions

The fluxes and velocity spectra for protons, deuterons and tritons produced in a PMMA target irradiated with a 220 MeV/u ^{12}C beam were measured at 60° and 90° with respect to primary beam direction. Furthermore, the spatial distribution of the fragments has been characterized to investigate a possible correlation between its shape and the dose profile inside the target. The final goal of this work was to develop a real-time technique based on the emission profile of charged secondary particles for monitoring the position of the irradiated volume in a patient during a hadrontherapy treatment.

One of the key parameters that had to be measured to validate the monitoring technique was the absolute resolution achievable on the released dose position. The results presented in this paper cover two different setup configurations, with the beam at 60° and 90° with respect to the monitoring device. The two setups are sensitive to different contributions to the resolution: while geometries closer to the primary beam direction have larger statistics and harder track momentum spectra, which leads to reduced MS contribution, the configurations at larger angles can exploit a better reconstruction geometry and profit from a MS effect that is reduced by the smaller path traversed by the charged particle inside the target.

An important conclusion that can be drawn from the measurements of the emission shape reported in this paper is that the experimental single track resolution needed for charged secondary track based monitoring techniques can be safely of the order of few millimeters without spoiling the high precision achievable on the longitudinal shape. The use of expensive, high resolution solid state detector seems then unnecessary, since the MS of the charged secondary particles in the patient exceeds few millimeters.

The precision obtained on the measured parameters that are shown to be correlated with the spatial positioning of the dose release was benchmarked using a reference sample made

of 10^3 tracks, compatible with what can be collected for few pencil beams in routine patient treatments. The presented results should be then considered as part of a preliminary attempt to assess the feasibility of a practical application of this technique to the clinical routine.

However, in real clinic applications we do expect a worsening of the resolution achievable due to the MS increase and to the heavily reduced charged particle statistics that can escape from the tissues. The impact of the low statistics could be reduced if a larger sample could be collected by a dedicated device whose angular acceptance could be very easily increased by almost a factor 50 with respect to our setup.

A crucial step in order to use charged secondary particles for monitoring purposes is a careful calibration of the relationship between the measured δ_{40} and Δ_{40} and the actual Bragg peak position at all beam energies of interest. These measurements will be useful both as a direct calibration of the device and to train the corresponding MC simulation.

The measured performances suggest the possibility to use the charged secondary emission shape as a monitoring tool in hadrontherapy. The comparison between this method and other proposed techniques, as prompt or γ-PET monitoring, depends on the actual details of the monitoring devices that exploit these different secondary flux, as acceptance and/or resolution.

In principle, the main advantages of the charged secondary monitoring with respect to the γ-PET, is the prompt feedback that can be provided to correct on-line the geometrical parameters of the treatment. The possibility to have a very high detection efficiency with respect to prompt photons seems to largely overcome the lower charged secondary yield per impinging beam particle with respect to the photons.

On the other hand, the most severe limitation seems to be the limited kinetic energy range of the produced charged secondary particles: only the very high tails of the energy distribution of these secondaries would emerge from a deep seated tumor (i.e. in the center of the head), reducing the signal sample. Since the range effect is less important in the carbon ion beam treatment, due to the harder energy spectra of the charged particle produced, the use of charged particle based monitors seems anyhow very promising for carbon ion beam therapeutic centers, while the application to proton beam needs further investigations.

Acknowledgments

We would like to thank Marco Magi (SBAI Department) for his valuable help in the construction of the mechanical support and Marta Rovituso (GSI) for her collaboration during the experiment. This work has been partly supported by the ‘Museo storico della Fisica e Centro di studi e ricerche Enrico Fermi’.

References

Abou-Haidar Z *et al* 2012 Performance of upstream interaction region detectors for the FIRST experiment at GSI *J. Instrum.* **7** 02006

Agodi C *et al* 2012a Precise measurement of prompt photon emission for carbon ion therapy *J. Instrum.* **7** 03001

Agodi C *et al* 2012b Charged particle’s flux measurement from PMMA irradiated by 80 MeV/u carbon ion beam *Phys. Med. Biol.* **57** 5667

Agodi C *et al* 2012c Study of the time and space distribution of beta+ emitters from 80 MeV/u carbon ion beam irradiation on PMMA *Nucl. Instrum. Methods Phys. Res.* B **283** 1–8

Amaldi U and Kraft G 2005 Radiotherapy with beams of carbon ions *Rep. Prog. Phys.* **68** 1861

Attanasi F *et al* 2009 Comparison of two dedicated in beam PET systems via simultaneous imaging of ^{12}C-induced β^+-activity *Phys. Med. Biol.* **54** 29

Battistoni G *et al* 2007 The FLUKA code: description and benchmarking *AIP Conf. Proc.* **896** 31–49

Bellini F *et al* 2014 Extended calibration range for prompt photon emission in ion beam irradiation *Nucl. Instrum. Methods Phys. Res.* A **745C** 114
Durante M and Loeffler J 2010 Charged particles in radiation oncology *Nature Rev. Clin. Oncol.* **7** 37
Enghardt W *et al* 2004 Charged hadron tumour therapy monitoring by means of PET *Nucl. Instrum. Methods Phys. Res.* A **25** 284
Ferrari A, Sala P, Fassò A and Ranft J 2005 FLUKA: a multi particle transport code *Technical Report* CERN-2005-10 vol INFN/TC05/11
Fiedler F *et al* 2008 In-beam PET measurements of biological half-lives of ^{12}C irradiation induced β^+-activity *Acta Oncol.* **47** 1077
Gwosch K *et al* 2013 Non-invasive monitoring of therapeutic carbon ion beams in a homogeneous phantom by tracking of secondary ions *Phys. Med. Biol.* **58** 3755
Henriquet P *et al* 2012 Interaction vertex imaging (IVI) for carbon ion therapy monitoring a feasibility study *Phys. Med. Biol.* **54** 4655
Jakel O, Karger C and Jurgen D 2008 The future of heavy ion radiotherapy *Med. Phys.* **35** 5653
Knopf A and Lomax A 2013 *In vivo* proton range verification: a review *Phys. Med. Biol.* **58** 131–60
Koba Y *et al* 2011 Scintillation efficiency of inorganic scintillators for intermediate-energy charged particles *Prog. Nucl. Sci. Technol.* **1** 218
Min C, Kim C Hyeong, Youn M and Kim J 2006 Prompt gamma measurements for locating the dose falloff region in the proton therapy *Appl. Phys. Lett.* **89** 183517
Mosegaard K and Tarantola A 2002 Probabilistic approach to inverse problems *International Handbook of Earthquake and Engineering Seismology (Part A)* vol 237 (New York: Academic)
Parodi K, Enghardt W and Haberer T 2002 In-beam PET measurements of β^+ radioactivity induced by proton beams *Phys. Med. Biol.* **47** 21
Pawelke J *et al* 1997 In-beam PET imaging for the control of heavy-ion tumour therapy *IEEE Trans. Nucl. Sci.* **44** 1492
Schardt D, Elsasser T and Schulz-Ertner D 2010 Heavy-ion tumor therapy: physical and radiobiological benefits *Rev. Mod. Phys.* **82** 383
Testa E *et al* 2008 Monitoring the Bragg peak location of 73 MeV/u carbon ions by means of prompt γ-ray measurements *Appl. Phys. Lett.* **93** 093506
Testa E *et al* 2009 Dose profile monitoring with carbon ions by means of prompt-gamma measurements *Nucl. Instrum. Methods Phys. Res.* B **267** 993
Vecchio S, Attanasi F, Belcari N and Camarda M 2009 A PET prototype for in-beam monitoring of proton therapy *IEEE Trans. Nucl. Sci.* **56** 1